

Internal wave beam propagation in nonuniform stratifications

MANIKANDAN MATHUR¹ AND THOMAS PEACOCK¹
†

¹Department of Mechanical Engineering, 77 Massachusetts Avenue, Cambridge, MA 02139,
USA

(Received 10 June 2009)

In addition to being observable in laboratory experiments, internal wave beams are reported in geophysical settings, which are characterized by nonuniform density stratifications. Here, we perform a combined theoretical and experimental study of the propagation of internal wave beams in nonuniform density stratifications. Transmission and reflection coefficients, which can differ greatly for different physical quantities, are determined for sharp density-gradient interfaces and finite-width transition regions, accounting for viscous dissipation. Thereafter, we consider even more complex stratifications to model geophysical scenarios. We show experimentally that wave beam ducting can occur under conditions that do not necessitate evanescent layers. Comparisons between the theory and quantitative experimental measurements of these processes show excellent agreement. Insights into wave beam observations at the Keana ridge, Hawaii are given within the context of these ideas.

† Corresponding author, e-mail: tomp@mit.edu

1. Introduction

Internal waves are propagating disturbances of the density stratification of a stably-stratified fluid. When generated by oscillatory flow relative to an obstacle, linear internal waves form beams, whose orientation is given by $\sin \theta = \omega/N$, where θ is the angle the beams make with a horizontal coordinate perpendicular to gravity g , ω is the forcing frequency, $N = \sqrt{-\frac{g}{\rho_0} \frac{d\rho}{dz}}$ is the local buoyancy frequency, $d\rho/dz$ is the local vertical density gradient and ρ_0 is a characteristic density of the fluid. The best known example is the St. Andrews Cross generated by an oscillating cylinder (Mowbray & Rarity 1967). Internal wave beams are not restricted to the laboratory, however, and are also reported in the ocean (e.g. Lien & Gregg 2001, Martin *et al.* 2006, Cole *et al.* 2009) and the atmosphere (e.g. Alexander *et al.* 1995, Walterscheid *et al.* 2001).

In geophysical settings, internal waves encounter significant variations in the stratification; examples include the thermocline in the ocean and evanescent regions in the mesosphere. To understand the impact of sudden changes in the stratification, Delisi & Orlanski (1975) investigated internal wave reflection from a density (and density-gradient) discontinuity. With the atmosphere in mind, Sutherland & Yewchuk (2004) derived an analytic prediction for plane internal waves traversing a sharply-defined layer of stronger stratification. This analysis was extended by Brown & Sutherland (2007) and Nault & Sutherland (2007), the latter considering plane waves propagating through a medium changing continuously from one stratification to another.

While there have been several recent experimental studies on internal wave beams in uniform stratifications (e.g. Peacock & Tabaei 2005, Zhang *et al.* 2007, Gostiaux & Dauxois 2007, Peacock *et al.* 2008), the effect of a nonuniform stratification on an internal wave beam has not come under such scrutiny. A theoretical study of internal wave beams propagating in an arbitrarily stratified fluid was performed by Kistovich & Chashechkin

(1998). They presented the results of analysis for: a smoothly varying stratification to which the beam continuously adjusts; reflection from a critical level where $\omega = N$; and interaction with discontinuities in N . The only related experimental studies used internal wave beams as approximations of plane waves (Delisi & Orlanski (1975), Sutherland & Yewchuck (2004)).

Here, we present a detailed study of the fundamental problem of an internal wave beam propagating in a nonuniform stratification. In the process, the plane wave analysis of Nault & Sutherland (2007) is extended to the regime in which internal waves propagate into regions of stronger stratification. We also develop an analytical method that is not subject to the restrictions of Kistovich & Chashechkin (1998), enabling investigation of important regimes where the scale of a wave beam is comparable to the scale of variations in the stratification. This analysis is complemented by the first quantitative comparison between theory and laboratory experiments for these processes.

The organization of the paper is as follows. The transmission of internal wave beams across sharp and finite-width density-gradient interfaces is addressed in sections 2 and 3, respectively. More complex, nonlinear stratifications are then considered in section 4. A direct comparison between theory and laboratory experiments is presented in section 5, followed by a discussion of geophysical applications in section 6. Finally, conclusions are presented in section 7.

2. Wave beam transmission across a sharp density-gradient interface

Consider a linear, two-dimensional plane wave propagating upwards in a medium of uniform buoyancy frequency N_1 , encountering a sharp density-gradient interface above which the uniform buoyancy frequency is N_2 (density being continuous across the interface), as illustrated in figure 1. The fluid layers on either side of the interface extend to

infinity, and non-Boussinesq and viscous effects are ignored, as is background rotation.

The streamfunctions ψ_I , ψ_R and ψ_T associated with the incident (I), reflected (R) and transmitted (T) waves are:

$$\psi_I = \Re(\Psi_I e^{[ik(x-z \cot \theta_1) - i\omega t]}), \quad (2.1)$$

$$\psi_R = \Re(\Psi_R e^{[ik(x+z \cot \theta_1) - i\omega t]}), \quad (2.2)$$

$$\psi_T = \Re(\Psi_T e^{[ik(x-z \cot \theta_2) - i\omega t]}), \quad (2.3)$$

where Ψ_I , Ψ_R and Ψ_T are complex amplitudes, \Re denotes the real part, x and z are the horizontal and vertical directions, and k the horizontal wavenumber. The angles $0 < \theta_1, \theta_2 < \pi/2$ are defined with respect to the x -axis, and the direction of energy propagation is further set by the sign of the coefficient of z in the exponent. The horizontal and vertical velocities are $u = \frac{-\partial\psi}{\partial z}$ and $w = \frac{\partial\psi}{\partial x}$, respectively. The pressure and density perturbations, p' and ρ' , are related to the streamfunction by $\frac{\partial^2 p'}{\partial x^2} = \rho_0 \frac{\partial^3 \psi}{\partial x \partial z \partial t}$ and $\frac{\partial \rho'}{\partial t} = \frac{\rho_0 N^2}{g} \frac{\partial \psi}{\partial x}$, respectively.

Applying continuity of vertical velocity and pressure at the density-gradient interface $z = 0$ gives transmission coefficients for different physical quantities. For example,

$$T_e = \frac{4 \cot \theta_1 \cot \theta_2}{(\cot \theta_1 + \cot \theta_2)^2}, \quad (2.4)$$

$$T_u = \frac{2 \cot \theta_2}{\cot \theta_1 + \cot \theta_2}, \quad (2.5)$$

$$T_w = \frac{2 \cot \theta_1}{\cot \theta_1 + \cot \theta_2}, \quad (2.6)$$

$$T_{\Delta N^2} = \frac{2 \cot \theta_2}{\cot \theta_1 + \cot \theta_2} \frac{\sin^2 \theta_1}{\sin^2 \theta_2}, \quad (2.7)$$

where T_e , T_u , T_w and $T_{\Delta N^2}$ are respectively the transmission coefficients for energy, e , the horizontal velocity, u , the vertical velocity, w , and $\Delta N^2 = \frac{-g}{\rho_0} \rho'_z$, ρ'_z being the vertical density gradient perturbation. The definition of T_e accounts for the geometric focusing of

internal wave energy, illustrated in figure 1. Since T_e is symmetric (i.e. unchanged upon interchanging θ_1 and θ_2), the fraction of the incident energy transmitted for a plane wave of frequency ω and horizontal wavenumber k is independent of whether it is passing from N_1 to N_2 , or the reverse. The coefficients T_w and $T_{\Delta N^2}$ are not symmetric, however, and hence depend on whether the transmission is from N_1 to N_2 , or vice versa. Some of the transmission coefficients are bounded (e.g. $T_e \leq 1$, $T_w \leq 2$), whereas others are not (e.g. $0 < T_{\Delta N^2} < \infty$) and hence the corresponding quantities can experience great amplification or diminution.

Before proceeding to study wave beams, an important piece of information is to know whether a plane wave can become unstable upon passing from one stratification to another. To investigate, first consider the net vertical density gradient, which is the sum of the background value $\frac{d\bar{\rho}}{dz}$ and the perturbation $\frac{\partial \rho'}{\partial z}$. For a plane wave that passes into the N_2 medium, the maximum value of this combination in the N_2 medium is:

$$\left(\frac{-\rho_0 N_2^2}{g}\right) \left[1 - \frac{k^2 |\Psi_I| \cot \theta_1}{N_1 \sin \theta_1} \frac{2 \cot \theta_2}{\cot \theta_1 + \cot \theta_2}\right]. \quad (2.8)$$

Assuming that the incident wave is linear and gravitationally stable, which requires $|\frac{\Delta N_I^2}{N_1^2}|_{max} = \frac{k^2 |\Psi_I| \cot \theta_1}{N_1 \sin \theta_1} \ll 1$, it is not possible for gravitational instability (i.e. $\frac{d\bar{\rho}}{dz} + \frac{\partial \rho'}{\partial z} > 0$) to arise upon transmission since $\frac{2 \cot \theta_2}{\cot \theta_1 + \cot \theta_2} \leq 2$. To consider shear-driven instability, one turns to the Richardson number $Ri = \frac{N^2}{(\partial u / \partial z)^2}$, for which a widely used instability criterion based on the properties of linear shear flow is $Ri < 1/4$ (Drazin & Reid 1981). While it is possible for the minimum Richardson number of a plane wave to be reduced on passing through a sharp density-gradient interface, increasing the likelihood of shear-driven instability, a gravitationally-stable linear plane wave cannot be shear-unstable (Thorpe 1999).

The results for plane waves extend to inviscid wave beams by following the lead of Kistovich & Chashechkin (1998) and Tabaei & Akylas (2003), and constructing the

stream function for a unidirectional wave beam using a linear superposition of plane waves (i.e. a Fourier decomposition of the wave field):

$$\psi(x, z, t) = \Re(e^{-i\omega t} \int_0^\infty \Psi_I(k) e^{ik(x-z \cot \theta)} dk), \quad (2.9)$$

where $\Psi_I(k)$ is the spectrum of the streamfunction for the wave beam. The cross-beam coordinate is $(x - z \cot \theta)$ and integration is over positive values of k , enforcing that the energy flux of the component plane waves is always up and to the right. The corresponding spectra for other physical quantities can be determined via the governing linear equations. For example, the spectra for u , w , p' and ρ'_z are $U_I(k) = -ik \cot \theta \Psi_I(k)$, $W_I(k) = -ik \Psi_I(k)$, $P_I(k) = -i\rho_0 \omega \cot \theta \Psi_I(k)$ and $D_I(k) = -\frac{i\rho_0 \omega}{g} \frac{k^2 \cot \theta}{\sin^2 \theta} \Psi_I(k)$, respectively.

In using a summation of plane waves to construct a wave beam, one must determine whether the resulting wave beam is both gravitationally and shear stable. By definition, a gravitationally stable wave beam in a background stratification N_0 has $\frac{\Delta N^2}{N_0^2} < 1$ throughout. For a linear wave beam, this condition also requires that the wave beam be shear stable, as shown in Appendix A.

Since plane wave transmission and reflection coefficients are independent of k for a sharp density-gradient interface, these coefficients are the same for a wave beam as a whole. Figures 2(a)-(d) present theoretical snapshots of four different physical quantities for a wave beam with $\Psi_I(k) \propto k e^{-k^2/c}$ at an arbitrarily chosen phase. The arrangement has $\omega/N_1 = 0.94$ and $N_2/N_1 = 3.2$, giving $T_u = 1.8$, $T_w = 0.2$, $T_{\Delta N^2} = 18.4$ and $T_e = 0.36$. In each figure, the physical quantity has been scaled so that the maximum value is unity. Figures 2(a)-(d) show u , w , ΔN^2 and the magnitude of the time-averaged energy flux, $\bar{e} = |\langle p(u, w) \rangle|$, respectively. The vertical velocity w is diminished, whereas u and ΔN^2 are amplified, upon transmission. The value of \bar{e} is enhanced by the geometric focusing of the beam, but only 36% of the overall incident energy flux is transmitted.

As is the case for a plane wave, the stability of a wave beam upon transmission is

determined by its effect on the stratification, since the general result that a gravitationally stable wave beam is shear stable still applies. Thus if $\frac{\Delta N^2}{N_0^2} \ll 1$ throughout the incident beam, this beam cannot become unstable. If $\frac{\Delta N^2}{N_0^2}$ is finite in the incident beam, linear theory no longer applies, and instability upon transmission is a possibility.

3. Wave beam transmission across a finite-width transition region

To understand the effect of a finite-width transition region on an internal wave beam, we first consider a plane wave propagating through the stratification

$$N^2 = \frac{N_2^2 - N_1^2}{2} \tanh\left(\frac{z}{L}\right) + \frac{N_1^2 + N_2^2}{2}, \quad (3.1)$$

shown in figure 3. Adopting the approach of Nault & Sutherland (2007), reflection and transmission coefficients can be calculated for periodic plane waves of frequency ω by defining $\psi = \Re(\phi(z)e^{i(kx-\omega t)})$ and solving the inviscid equation,

$$\phi'' + k^2\left(\frac{N^2}{\omega^2} - 1\right)\phi = 0, \quad (3.2)$$

where k , like ω , is assumed to be real, and the prime denotes differentiation with respect to z . An upward-propagating plane wave of unit amplitude in the N_1 layer results in a downward-propagating reflected wave in the N_1 layer and an upward-propagating transmitted wave in the N_2 layer. Thus, the general solutions in the N_1 and N_2 layers, respectively, are:

$$\phi_1 = e^{m_1 z} + A e^{m_2 z}, \quad (3.3)$$

$$\phi_2 = C e^{n_1 z}, \quad (3.4)$$

where the vertical wave numbers in the lower and upper constant stratifications are $m_1 = -m_2 = -k \cot \theta_1$ and $n_1 = -k \cot \theta_2$, respectively. The energy transmission coefficient is

$$T_e = |C|^2 \frac{n_1}{m_1}, \quad (3.5)$$

and the corresponding reflection coefficient is $R_e = |A|^2$. It is found that, for a given k and ω , T_e is independent of whether a wave passes from N_1 to N_2 or vice-versa. In general, T_e strongly depends on ω/N_1 , N_2/N_1 and the ratio of the transition length L to the vertical wavelength of the plane wave, which can change significantly on transmission.

Figures 4(a) and (b) present T_e as a function of ω/N_1 and N_2/N_1 for $Lk = 0.1$ and $Lk = 1$, respectively. As the transition region increases in thickness relative to the vertical wavelength there is increased transmission for all ω/N_1 and N_2/N_1 . Roughly speaking, near perfect transmission occurs when the maximum vertical wavelength in the N_1 or N_2 layers is much smaller than L , i.e.

$$Lk \min(\cot \theta_1, \cot \theta_2) \gg 1. \quad (3.6)$$

More precisely, if $Lk \min(\cot \theta_1, \cot \theta_2) > 1$, leading order WKB theory predicts energy transmission to within 10% for all but the cases where $|\theta_1 - \theta_2| > 84^\circ$. To illustrate this, contours of $Lk \min(\cot \theta_1, \cot \theta_2) = 0.5, 1$ are included in figures 4(a) and (b). These results are consistent with Nault & Sutherland (2007), who studied the case $N_2 < N_1$. At the other extreme, the transmission process is akin to a sharp density-gradient interface when the smallest vertical wavelength in the N_1 or N_2 layers is significantly larger than L , i.e.

$$Lk \max(\cot \theta_1, \cot \theta_2) \ll 1. \quad (3.7)$$

Indeed, if $Lk \max(\cot \theta_1, \cot \theta_2) < 0.1$, sharp-interface theory correctly predicts energy transmission to within 1%.

To compute the transmission of an inviscid wave beam encountering a finite-width N_1 -to- N_2 transition region, the streamfunction of the incident beam is again represented as the Fourier sum (2.9). For a given $\Psi_I(k)$, the spectra $\Psi_T(k)$ and $\Psi_R(k)$ must be computed using (3.2) to determine transmission and reflection for each constituent wave number k .

The nature of the transmitted and reflected beam profiles is determined by the details of the transition region, which acts as a high-pass filter that allows large wavenumbers to transmit completely (3.6). This is illustrated in figure 5, which presents results for an incident wave beam with $\omega/N_1 = 0.94$, comprising equal amounts of energy in two bands of wavenumbers, one centered around $kL = 0.1$ and the other around $kL = 0.7$. Figure 5(a) presents a snapshot of the horizontal velocity field for $N_2/N_1 = 10$, in which it is apparent that the transmitted beam is much finer in scale than the incident beam. Furthermore, the reflected beam is noticeably weaker than the incident beam, indicating that significant energy flux is passing through the interface. The transmitted beam is finer in scale not only because of focusing by a stronger stratification, but also due to filtering by the finite-width transition region. This filtering process, where the large wavenumbers transmit completely (3.6) and the small wavenumbers follow the sharp-interface results (3.7), is elucidated in figures 5(b) and (c), which plot the energy flux transmission and reflection coefficients as a function of Lk , and the energy spectra $|E(k)| = k|\Psi|^2 \cot \theta$ of the incident, transmitted and reflected beams. As a consequence of the variations of T_e and R_e with Lk , the reflected and transmitted wave beam spectra are strong at relatively small and large values of Lk , respectively.

For the purpose of comparison with experiments in section 5, we consider the full viscous equation:

$$\phi'' + k^2 \left(\frac{N^2}{\omega^2} - 1 \right) \phi = \frac{i\nu}{\omega} \left(\phi'''' - 2k^2 \phi'' + k^4 \phi \right), \quad (3.8)$$

where ν is the kinematic viscosity, and k and ω are again real. The Schmidt number, which represents the ratio of momentum diffusivity (dynamic viscosity) and mass diffusivity, is assumed to be infinite. The above fourth order equation requires four boundary conditions for a unique solution. It is not practical to solve the equation as an initial value problem (satisfying all four boundary conditions at $z = -\infty$ or $z = +\infty$), because it has a pair of

rapidly growing and decaying viscous solutions that cause numerical instability. Instead, this is best solved as a boundary value problem (satisfying two boundary conditions each at $z = -\infty$ and $z = +\infty$), which requires four boundary conditions. To express the boundary conditions in terms of ϕ , ϕ' , ϕ'' and ϕ''' , an incident, weakly damped, upward-propagating wave of unit amplitude in the N_1 layer is assumed. This can generate a pair of reflected, downward-propagating waves in the N_1 layer, one weakly damped and the other strongly damped; and a pair of transmitted, upward-propagating waves in the N_2 layer, one weakly damped and the other strongly damped. Thus, the general solutions in the N_1 and N_2 layers, respectively, are:

$$\phi_1 = e^{m_1 z} + Ae^{m_2 z} + Be^{m_3 z}, \quad (3.9)$$

$$\phi_2 = Ce^{n_1 z} + De^{n_2 z}. \quad (3.10)$$

The coefficients A , B , C and D are the unknown reflection and transmission amplitudes, and the exponents m_i and n_i are obtained by solving (3.8) in the constant stratification regions, keeping only modes that decay in the upward and downward directions for the upper and lower layers, respectively. To further clarify the directions of viscous decay in the two layers, we point out that $\Re(m_1) < 0$, $\Re(m_2, m_3) > 0$, $m_2 = -m_1$ and $\Re(n_1, n_2) < 0$. Expressions for ϕ_1 , ϕ'_1 , ϕ''_1 and ϕ'''_1 in the N_1 layer are reduced to two boundary conditions by eliminating the unknown constants A and B . A similar procedure to eliminate the unknown constants C and D gives two boundary conditions in the upper N_2 layer. The boundary value problem is now numerically solved in Matlab using the function *bvp4c*.

4. Wave beam propagation in complex stratifications

4.1. Multiple sharp density-gradient interfaces

When a wave beam encounters a series of sharp density-gradient interfaces, multiple reflections and transmissions occur. Two canonical scenarios are presented in figures 6(a) and (b), respectively. In the sketch in figure 6(a), a finite depth N_2 -layer lays between two semi-infinite N_1 -layers. Determining the amplitudes of reflected and transmitted wave beams that result from an upward-propagating incident wave beam requires the imposition of boundary conditions on vertical velocity and pressure at $z = -H, H$ for the constituent plane waves (Gill 1982, Sutherland & Yewchuk 2004). A related arrangement, presented in figure 6(b), is a finite-depth N_2 -layer sitting atop a semi-infinite N_1 -layer, above which is a rigid boundary. To obtain a solution here requires imposition of boundary conditions at $z = 0, -H$. The resulting wave field is related by symmetry to that in figure 6(a), as indicated. Scenarios with multiple finite-depth layers can be solved using the same approach, with the imposition of boundary conditions becoming more laborious as the number of layers increases.

Focusing on the scenario in figure 6(b), all the energy in the incident wave beam is ultimately reflected back to the N_1 -layer, irrespective of the values of ω/N_1 and N_2/N_1 . As will be shown, however, energy can be ducted for quite some distance. An important parameter for this configuration is the ratio of the horizontal distance $L^* = 2H \cot \theta_2$ to the horizontal width of an incident wave beam L_h . If $L^*/L_h > 1$, neighboring reflected wave beams do not interfere with each other. In this case, the fraction of incident energy returned in the n^{th} downward-propagating beam, given that T_e is symmetric with respect to an interchange between N_1 and N_2 , is $\alpha_n = R_e^{n-2} T_e^2$ for $n \geq 2$, where $R_e = 1 - T_e$; for $n = 1$, $\alpha_1 = R_e$. The fraction of incident energy remaining in the N_2 -layer after the emergence of $n \geq 2$ downward beams has a maximum value of $\frac{(n-1)^{n-1}}{n^n}$ for $T_e = \frac{1}{n}$. To

maximize the remaining energy for $n = 2, 3, 4, 5$, the values of T_e must therefore be 0.5, 0.33, 0.25 and 0.2, respectively; for which the fraction of incident energy remaining is 0.25, 0.15, 0.11 and 0.082, respectively. When $L^*/L_h \approx 1$, there is no longer a sequence of re-emerging individual beams, but rather a more broadly scattered wave field. Finally, the case $L^*/L_h \ll 1$ is equivalent to the N_2 -layer being absent, and for all practical purposes there is a solid boundary that reflects the wave beam. In this limit, if L_h is also much larger than the characteristic horizontal wave length in the wave beam, the reflection process becomes akin to that of a plane wave.

To elucidate these scenarios, in figure 7 we plot the cumulative re-emerging energy flux across the interface e_c (normalized by the energy flux in the incident wave beam) as a function of x/L_h . For this example, $\omega/N_1 = 0.5$ and $N_2/N_1 = 2.8$, giving $T_e = 0.73$. For $L^*/L_h > 1$, the re-emerging beams are distinct, giving rise to rapid increases in e_c at specific locations. The interference between neighboring wave beams for $L^*/L_h \approx 1$ produces a more continuous spatial variation of e_c . For a thin N_2 -layer, there is essentially only a single reflected beam originating from the initial reflection site. For all the cases studied, at least 70% of the incident energy is reflected back to the N_1 -layer by $x/L^* = 2$, although this can occur in the different ways just described. For $L^*/L_h > 1$, either the first or second reflected wave beam contains most of the energy, depending on whether $T_e > 0.62$ or $T_e < 0.62$, respectively.

4.2. Continuous stratifications

It is readily possible to study complex, continuous stratifications using the approach detailed in section 3. To represent the upper-ocean better, for example, a natural extension of the configuration in figure 6(b) that accounts for the thermocline and mixed-layer is to introduce a finite-width N_1 -to- N_2 transition and a uniform density layer atop the N_2 -layer. This problem can be solved using equation (3.3), with or without viscosity, by

specifying boundary conditions at the upper rigid boundary and for reflected waves in the N_1 layer. For this scenario, however, it was actually found to be computationally faster to exploit the symmetry identified in figure 6(a). The results presented in the following section were therefore obtained by solving for the configuration in 6(a) and then forming the solution $\psi^*(x, z, t) = \psi(x, z, t) - \psi(x, -z, t)$ for $z < 0$.

5. Experiments

5.1. Apparatus

To complement the analysis of the previous sections, we performed experiments in a 1.28 m-long, 0.66 m-high and 0.2 m-wide acrylic tank, with 19 mm-thick walls. The tank was filled from below with salt water and stratified using the double-bucket method. Nonlinear stratifications with mm-scale transition regions were achieved using computer-controlled peristaltic pumps, which enabled precise control of the flow rates within, and out of, the double bucket system. If desired, the transition regions were sharpened by slowly and selectively withdrawing fluid via a syringe. A calibrated PME conductivity and temperature probe, mounted on a linear traverse, was used to measure the resulting density profile prior to an experiment. Blocksom-filter matting, a coarse coconut-hair matting, effectively damped reflections of internal wave beams from the side walls.

An internal wave beam was produced using a generator based on the design of Gostiaux *et al.* (2007). The generator, comprising twelve oscillating plates, could be oriented to point downwards at an angle $0^\circ < \theta < 45^\circ$ with respect to the horizontal. The motion of the plates was driven using a computer-controlled stepper motor. A nice feature of a generator such as this is the ability to produce a single internal wave beam, with accurate control of the frequency of oscillation (and thus propagation direction) and cross-beam profile (and thus dominant wavelength). The profile used for these experiments

had a maximum oscillation amplitude of 8 mm for the central plates, which tapered smoothly to zero at the top and bottom plates. This arrangement produced a wave beam with a roughly gaussian spectrum for $D_I(k)$ that peaked at around $k_0 = 100 \text{ m}^{-1}$ for the experiments discussed here and decayed to half the peak value within the range $k = k_0 \pm 55 \text{ m}^{-1}$.

Internal wave beams were visualized using the Synthetic Schlieren method (Dalziel *et al.* 2000). A random pattern of mm-scale dots, backlit by an electroluminescent sheet, was positioned 1.25 m behind the experimental tank. A JAI CV-M4+ CCD camera, located 3.18 m in front the tank, was used to record apparent distortions of the dot pattern. These distortions were processed using DigiFlow (Dalziel 2009), to obtain spatiotemporal data of density-gradient perturbations within the stratification.

5.2. Results

The density profile for the first experiment is presented in figure 8(a). This comprised an approximately 2 cm-wide strong stratification layer between an upper, linear stratification and an underlying, 10 cm-high constant-density layer. The constant-density layer was included for practical purposes: to aid visualization, to reduce erosion of the stratification layer from below by diffusion, and to permit several selective withdrawal procedures. It played a passive role in the experiments. The corresponding N -profile, computed from the experimentally measured density profile in figure 8(a), is presented in figure 8(b). The maximum stratification was $N_{\max} = 1.44 \text{ s}^{-1}$, while $N_1 = 0.89 \text{ s}^{-1}$ in the upper, constant stratification .

An experimental Synthetic Schlieren visualization for a wave beam with $\omega/N_1 = 0.82$ propagating in the stratification in figure 8(b) is presented in figure 8(c). This image was obtained 128 seconds after the wave generator was started, allowing sufficient time for the wave field to achieve a periodic state. The phase of oscillation was chosen arbitrarily, since

the qualitative picture was the same at any phase during the cycle. For this configuration, neighboring reflected wave beams overlap, resulting in a continuously distributed wave field scattered back into the N_1 medium, with a detectable signal as far away as three times the horizontal width of the incident wave beam.

To relate this experiment to the simple model in figure 6(b), the system can be approximated as having a semi-infinite upper layer of constant stratification $N_1 = 0.89 \text{ s}^{-1}$ and a roughly 2 cm-thick layer of mean stratification $N_2 \approx 1.34 \text{ s}^{-1}$, separated by a transition layer L of mm-scale thickness. The passive, constant-density layer is treated as an inviscid solid boundary at the base of the N_2 layer. A dominant horizontal wave length of 7 cm in the spectrum $D_I(k) = -\frac{i\rho_0\omega}{g} \frac{k^2 \cot \theta}{\sin^2 \theta} \Psi_I(k)$ means that $Lk \cot \theta_2 \ll 0.1$, so a sharp interface approximation can be used for the N_1 -to- N_2 transition. For this scenario $T_e = 0.86$, meaning most of the incident energy gets transmitted to the N_2 -layer and hence a little ducting can take place. Since $L^* \sim 10 \text{ cm}$ is on the same scale as the horizontal width of the wave beam L_h , giving $L^*/L_h \sim 1$, there is a broadly scattered beam.

A more rigorous comparison of experiment and theory was sought by extracting the horizontal Fourier spectrum of the incident experimental wave beam. For each horizontal wave number, using a resolution of $\delta k = 0.1 \text{ m}^{-1}$, the corresponding vertical mode of the stratification was calculated using the viscous equation (3.8) with $\nu = 1.0 \times 10^{-6} \text{ m}^2\text{s}^{-1}$. This decomposition was used to reproduce the horizontal structure of the incident wave beam, and its accuracy was validated by checking that the vertical cross-sectional structure of the incident wave beam was also reproduced. Having obtained the decomposition, the propagation of the wave beam through the stratification was determined by plotting the incident and reflected wave fields for the horizontal extent of the experimental domain. The result is presented in figure 8(d), which shows good

agreement with the experimental data in 8(c). An even more direct comparison between theory and experiments is presented in figure 8(e), in which the local oscillation amplitude (i.e. the amplitude envelope) of ρ'_z is plotted for the horizontal cross section indicated in figures 8(c) and (d).

A second experiment was performed that required further selective withdrawal from $z \approx 0.144\text{m}$, after which the density profile was left to diffuse for ten hours. This produced the desired effect of widening the strong stratification layer and increasing the peak value of N in this layer. As shown in figures 9(a) and (b), N_{max} rose to 1.94 s^{-1} , and the layer thickness increased to around 4 cm.

In figure 9(c) we present an experimental Synthetic Schlieren visualization for a wave beam with $\omega/N_1 = 0.87$ propagating in the stratification in figure 9(b). As before, the phase of the oscillation was chosen arbitrarily once the system had achieved a periodic state. For this configuration, two distinct wave beams are scattered back into the N_1 medium. The second wave beam, which emerges from the strong-stratification layer around $x = 0.25 \text{ m}$, is significantly stronger than the first, which is reflected around $x = 0.08 \text{ m}$. There is also significant activity in the N_2 -layer all the way to $x = 0.4 \text{ m}$, corresponding to horizontal ducting of the wave beam.

This arrangement can also be reasonably approximated as a two layer system, with an upper semi-finite layer where $N_1 = 0.89 \text{ s}^{-1}$ and a 4 cm-thick layer with $N_2 \approx 1.62 \text{ s}^{-1}$, separated by a sharp interface. This gives $T_e = 0.72$, which is reasonable for ducting and causes the second reflected beam to be significantly stronger than the first, consistent with experimental observations. Because of the thicker layer and stronger stratification compared to the previous experiment ($L^*/L_h > 2$), distinct scattered wave beams were produced. The Fourier decomposition method was also used to obtain a more rigorous comparison of experiment and theory for this configuration. The corresponding

theoretical result is presented in figure 9(d), which is in agreement with the experimental results in figure 9(c). The level of agreement is further demonstrated by the plot in figure 9(e), which presents the amplitude envelope for ρ'_z for the horizontal cross section indicated in figures 9(c) and (d).

In making the quantitative comparisons between laboratory experiments and theory, it was found that molecular viscosity provided significant damping in regions of strong stratification, due to the finer vertical wavelengths. This is understood by considering the viscous decay of a linear plane wave along its direction of propagation η , which is accounted for by the viscous decay factor $e^{-\alpha\eta}$, where $\alpha = \frac{\nu k^3 N^3}{2\omega^3 \sqrt{N^2 - \omega^2}}$ (Lighthill 1978). For the experimental results presented in figures 8(c) and 9(c), the decay coefficient α was roughly 1.55 and 1.86 times greater in the N_2 layer than in the N_1 region, respectively.

6. Discussion

The methods developed and implemented herein provide a means to investigate the effect of a nonlinear density stratification on the propagation of a linear internal wave beam. These methods can be useful for investigating geophysical scenarios. There are many such scenarios to consider (e.g. Alexander *et al.* 1995, Lien & Gregg 2001, Walterscheid *et al.* 2001, Cole *et al.* 2009), and we choose the example of a semidiurnal wave beam at the Keana ridge in the Kauai channel of the Hawaiian islands (Martin *et al.* 2006). As shown in figure 10(a), which is reproduced from Martin *et al.* (2006), the wave beam originated from the northern side of the ridge peak and struck the ocean surface 20 km south of the ridge peak. The physical quantity presented is the horizontal kinetic energy $E_K = \frac{1}{2}\rho_0 \langle u^2 + v^2 \rangle$, where v is the additional transverse horizontal velocity component required by background rotation. Directly atop the ridge, E_K has a maximum that extends for a horizontal distance of $\sigma \sim 25$ km, although this quantity

actually rises to a maximum and returns to zero over roughly twice this distance. Since E_K is quadratic in the perturbation velocity, it emphasizes stronger activity along the center of a wave beam, so a reasonable width for the oceanic wave beam is $2\sigma \sim 50$ km. There appears to be no wave beam reflected back down from the surface.

Before investigating the role of stratification in this scenario, it is worth assessing whether the wave beam can be considered linear. At a depth of 500 m, the maximum value of E_K in the wave beam is roughly 25 Jm^{-3} , corresponding to $u, v \sim 0.1 \text{ ms}^{-1}$. For semidiurnal waves with $10^{-3} < k < 10^{-4} \text{ m}^{-1}$, consistent with the scale of the topography and the width of the wave beam, the horizontal and vertical momentum equations require that the values of $\frac{uk}{\omega}$ and $\frac{\Delta N^2}{N_0^2}$ both exceed 0.1. This implies that advection terms in the momentum equations and perturbations of the background stratification could be sufficiently large that nonlinearity is significant. With this in mind, we nevertheless proceed to discuss what linear theory can say.

A time-averaged and an individual density profile obtained from the Keana ridge at the time of the data in figure 10(a) are presented in figures 10(b) & 10(c), respectively. The averaged profile was calculated from thirty individual profiles taken at twenty-four hour intervals. The individual profile follows the same general trend as the averaged profile, but has small scale features. Some of these features are strong, which is perhaps another indication of nonlinearity. These density profiles were used as the basis of simulations of a 50 km-wide wave beam. Background rotation was included by replacing $(N^2/\omega^2 - 1)$ by $(N^2 - \omega^2)/(\omega^2 - f^2)$ in (3.2), where f is the Coriolis parameter. This acts to reduce the propagation angle of the wave beam, thereby affecting transmission and reflection[†].

[†] For a sharp density-gradient interface between two regions of constant stratification N_1 and N_2 , the effect of background rotation may simply be accounted for by using the rotational dispersion relation (Peacock & Weidman 2005) to calculate the angles θ_1 and θ_2 for transmission and reflection coefficients such as (2.5).

Since a wave beam typically contains at least one, and perhaps several, spatial oscillations (Thomas & Stevenson 1972), simulations were run for different dominant horizontal wavelengths of 10 km, 15 km, 25 km and 50 km, as well as a mixed wave beam containing equal energy flux for these wavelengths. In each case, the magnitude of the perturbation velocity u was chosen to reproduce the magnitude of E_K in the field data in figure 10(a).

The results of the calculations for an internal wave beam with a 15 km dominant wave length are presented in figure 11, which also presents the calculated N -profiles. The quantity E_K increases as the beam rises through the stratification, consistent with the ocean observations. The averaged N -profile in figure 11(a) distorts the wave beam that originates from $x = 10$ km in figure 11(b), but ultimately there is a strong wave beam reflected back down from the surface. In contrast, the extra features in the individual stratification in figure 11(c) significantly distort the wave beam in figure 11(d), greatly weakening the reflected beam and creating a second site of surface activity, consistent with the field data in figure 10(a). Qualitatively similar behavior, albeit to varying degrees, was observed for the other simulations with different dominant wavelengths, suggesting that scattering by small scale features could have played a key role in the fate of the oceanic wave beam. This interpretation is in line with previous theoretical results for plane wave scattering by perturbations of the stratification (Barcilon *et. al.* 1972). It is also interesting to note that the field data, like the simulations, has vertically periodic structures with a scale of 100 m that are consistent with scattering by the stratification.

Another aspect of the wave beam worth considering is its stability. Even at a depth of 500 m linear scaling arguments suggest that $0.1 < \frac{\Delta N^2}{N_0^2} < 1$. In support of this, values of N approaching zero exist at a few points in the profiles in figure 11(c). This suggests that the wave beam was susceptible to gravitational instability. In figure 12 we plot the minimum value of the net stratification, $N_{\min}^2 = N_0^2 + \Delta N_{\min}^2$, for the wave beam dominated

by 15 km wavelengths. The result shows that the likelihood of gravitational instability increases significantly as the wave beam propagates upwards, reaching a maximum in the vicinity of the reflection site. For all the wave beams of various dominant wave lengths that we simulated, gravitational instability set in at some depth, this being shallower for wave beams comprising longer wave lengths. Therefore, in addition to scattering, it is likely that the wave beam became gravitationally unstable.

While instability may have been a significant cause of dissipation, we remark that the quantitative comparisons between experiment and theory in figures 8 and 9 revealed that theoretical scattered wave beams are considerably weaker if the viscous equation (3.8) is used rather than its inviscid counterpart (3.2). By analogy, pre-existing turbulent dissipation (Thorpe 2007) can also damp an oceanic wave beam. Recalling that the viscous decay factor for a linear plane wave is $e^{-\frac{\nu k^3 N^3}{2\omega^3 \sqrt{N^2 - \omega^2}} \eta}$, where η is the propagation distance, a back-of-the-envelope calculation shows that a turbulent viscosity of $\nu_T \sim 10^{-3} \text{ m}^2 \text{ s}^{-1}$ is sufficient to cause an order of magnitude decay of a 15 km wave traveling 20 km in a stratification $N_0 = 0.02 \text{ s}^{-1}$. This value of turbulent viscosity is within reason (Gill 1982), suggesting that the Hawaiian wave beam would also have been significantly damped by pre-existing upper-ocean conditions.

Finally, we note that ducting of plane internal waves in the presence of evanescent layers has been previously recognized in both the ocean (Eckart 1961) and atmosphere (Fritts & Yuan 1989, Walterscheid *et. al.* 2001). For the simple case of a constant- N layer (in which waves can propagate) between two evanescent layers, the two evanescent layers hinder energy from entering the constant- N layer; once inside, however, any energy has great difficulty escaping. The results in this paper demonstrate that stratifications with layers of relatively stronger N , but not necessarily with any evanescent layers, can support ducting too.

7. Conclusions

The propagation of an internal wave beam in a nonuniform stratification has been investigated using Fourier methods. When changes in the stratification occur on a relatively large scale, the wave beam retains its identity, adjusting continuously to the surrounding stratification. The changing stratification may significantly amplify or reduce the magnitude of physical quantities associated with the beam. If changes of the stratification occur on a relatively short scale, however, the wave beam is scattered. This process can be reasonably modeled using sharp density-gradient interfaces if changes in stratification occur on length scales an order of magnitude smaller than the smallest vertical wave length in the wave beam. For complicated stratifications, multiple transmitted and reflected beams, and internal wave beam ducting, can occur. This has been demonstrated in laboratory experiments, for which there was very good agreement with viscous, linear theory.

This work provides insight into geophysical wave beams. The complexity of the physical environments means that detailed and comprehensive field data is required to unambiguously identify the roles of scattering, instability and pre-existing turbulence in any particular situation. In such studies there are other candidate mechanisms, which lie beyond the scope of this paper, that could contribute to the understanding of field observations. The influence of background shear, for example, alters a wave beam slope, causes an exchange of energy with the mean-flow and promotes instability (Koop 1981, Koop & McGee 1986). The nonlinear generation of solitary waves (Gerkema 2001, Akylas *et al.* 2007) could also be important. With all these processes, typically one cannot expect a geophysical wave beam to remain intact as it propagates through a complex stratification.

We acknowledge helpful discussions with Neil Balmforth, Bruce Sutherland and Theo

Gerkema, and thank Rob Pinkel and Dan Rudnick for providing us with stratification data from the Kauai channel. We also thank Christopher Dimitriou for helping with construction of the wave generator. This work was supported by NSF grant 0645529 and ONR grant N00014-09-1-0282.

Appendix A. Richardson number for a wave beam

For an upward-propagating wave beam,

$$\left(\frac{\partial u}{\partial z}, \frac{\partial p'}{\partial z}\right) = \text{Re}(e^{-i\omega t} \int_0^\infty -k^2(\cot \theta, \frac{i\rho_0 N^2}{g\omega}) \Psi \cot \theta e^{ik(x-z \cot \theta)} dk). \quad (\text{A } 1)$$

Thus

$$Ri = \frac{N^2}{\cot^4 \theta (A^2 + B^2)} \frac{1 - f \sin \gamma}{\cos^2 \gamma}, \quad (\text{A } 2)$$

where $\int_0^\infty -ik^2 \Psi e^{ik(x-z \cot \theta)} dk = A(x, z) + iB(x, z)$, $\tan \phi = \frac{A}{B}$, $f = \frac{\cot \theta}{N \sin \theta} \sqrt{A^2 + B^2}$

and $\gamma = \omega t + \phi$. The value of γ at which Ri is minimum satisfies

$$\sin \gamma = \frac{1}{f} \pm \sqrt{\frac{1}{f^2} - 1}. \quad (\text{A } 3)$$

Now $f < 1$, as otherwise the numerator in (A 2) can be negative, corresponding to gravitational instability. Therefore, the relevant minimum is

$$Ri_{\min} = \frac{1}{2 \cos^2 \theta} \frac{1}{1 - \sqrt{1 - f^2}}. \quad (\text{A } 4)$$

This is greater than 1/2 for $f < 1$ and $\cos \theta < 1$, and thus shear-driven instability, which requires $Ri < 1/4$, cannot occur.

REFERENCES

- AKYLAS, T. R., GRIMSHAW, R. H. J., CLARKE, S. R. & TABAEI, A. 2007 Reflecting tidal wave beams and local generation of solitary waves in the ocean thermocline. *J. Fluid Mech.* **593**, 297–313.

- ALEXANDER, M. J., HOLTON, J. R. & DURRAN, D. R. 1995 The gravity wave response above deep convection in a squall line simulation. *J. Atmos. Sci.* **52**, 2212–2226.
- BARCILON, A., BLUMSACK, S. & LAU, J. 1972 Reflection of internal gravity waves by small density variations. *J. Phys. Ocean.* **2**, 104–107.
- BROWN, G. L. & SUTHERLAND, B. R. 2007 Internal wave tunnelling through non-uniformly stratified shear flow. *Atmos. Ocean* **45**, 47–56.
- COLE, S.T., RUDNICK, D.L., HODGES, B.A. & MARTIN, J.P. 2009 Observations of tidal internal wave beams at Kauai Channel, Hawaii. *J. Phys. Ocean.*, to appear.
- DALZIEL, S.B., HUGHES, G.O. & SUTHERLAND, B.R. 2000 Whole-field density measurements by ‘synthetic schlieren’. *Expts. Fluids* **28**, 322–335.
- DALZIEL, S.B. 2009 <http://www.damtp.cam.ac.uk/lab/digiflow/>.
- DELISI, D.P. & ORLANSKI, I. 1975 On the role of density jumps in the reflexion and breaking of internal gravity waves. *J. Fluid Mech.* **69**, 445–464.
- DRAZIN, P.G. & REID, W.H. 1981 Hydrodynamic Stability. *Cambridge University Press*, 323–327.
- ECKART, C. 1961 Internal Waves in the Ocean *Phys. Fluids*. **4**, 791–799.
- FRITTS, D.C. & YUAN, L. 1989 An analysis of gravity wave ducting in the atmosphere: Eckart’s resonances in thermal and Doppler ducts *J. Geophys. Research* **94**, NO. D15, 18,455–18,466.
- GERKEMA, T. 2001 Internal and interfacial tides: beam scattering and local generation of solitary waves. *J. Mar. Res.* **59(2)**, 227–255.
- GILL, A.E. 1982 Atmosphere–Ocean Dynamics. *Academic Press Inc.*
- GOSTIAUX, L. & DAUXOIS, T. 2007 Laboratory experiments on the generation of internal tidal beams over steep slopes *Phys. Fluids*, **19**, 028102.
- GOSTIAUX, L., DIDELLE, H., MERCIER, S., & DAUXOIS, T. 2007 A novel internal waves generator. *Expts. Fluids* **42**, 123–130.
- KISTOVICH, Y.V. & CHACHESHKIN, Y.D. 1998 Linear theory of the propagation of internal wave beams in an arbitrarily stratified liquid. *J. Appl. Mech. & Tech. Phys.* **39**, No. 5, 729–737.
- KOOP, C.G. 1981 A preliminary investigation of the interaction of internal gravity waves with a steady shearing motion *J. Fluid Mech.* **113**, 347–386.

- KOOP, C.G. & MCGEE, B. 1986 Measurements of internal gravity waves in a continuously stratified shear flow *J. Fluid Mech.* **172**, 453–480.
- LIEN, R.-C. & GREGG, M.C. 2001 Observations of turbulence in a tidal beam and across a coastal ridge. *J. Geophys. Res.* **106**, 4575–4591.
- LIGHTHILL, J. 1978 Waves in Fluids. *Cambridge University Press*, 4.10.
- MARTIN, J. P., RUDNICK, D.L. & PINKEL, R. 2006 Spatially broad observations of internal waves in the upper Ocean at the Hawaiian ridge *J. Phys. Ocean.* **36**, (6), 1085–1103.
- MOWBRAY, D.E. & RARITY, B.S.H. 1967 A theoretical and experimental investigation of the phase configuration of internal waves of small amplitude in a density stratified liquid. *J. Fluid Mech.* **28**, 1–16.
- NAULT, J. T. & SUTHERLAND, B. R. 2007 Internal wave transmission in nonuniform flows. *Phys. Fluids* **19**, 016601.
- PEACOCK, T. & TABAEI, A. 2005 Visualization of nonlinear effects in reflecting internal wave beams. *Phys. Fluids* **17**, 061702.
- PEACOCK, T. & WEIDMAN, P. 2005 The effect of rotation on conical wave beams in a stratified fluid. *Expts. Fluids* **39**, 32–37.
- PEACOCK, T., ECHEVERRI, P. & BALMFORTH, N.J.B. 2008 Experimental investigation of internal tide generation by two-dimensional topography. *J. Phys. Ocean.* **38**, 235–242.
- SUTHERLAND, B. R. & YEWCHUK, K. 2004 Internal wave tunnelling. *J. Fluid Mech.* **511**, 125–134.
- TABAEI, A. & AKYLAS, T.R. 2003 Nonlinear internal gravity wave beams. *J. Fluid Mech.* **482**, 141–161.
- THOMAS, N.H. & STEVENSON, T.N. 1972 A similarity solution for internal waves. *J. Fluid Mech.* **54**, 495–506.
- THORPE, S.A. 1998 Nonlinear Reflection of Internal Waves at a Density Discontinuity at the Base of the Mixed Layer. *J. Phys. Oceanogr.* **28**, 1853–1860.
- THORPE, S.A. 1999 On the breaking of internal waves in the ocean *J. Phys. Oceanogr.* **29**, 2433–2441.
- THORPE, S.A. 2007 An introduction to ocean turbulence. *Cambridge University Press*.

- WALTERSCHEID, R.L., SCHUBERT, G., & BRINKMAN, D.G. 2001 Small-scale gravity waves in the upper mesosphere and lower thermosphere generated by deep tropical convection *J. Geophys. Res.* **106**(D23), 31825–31832.
- ZHANG, H.P., KING, B. & SWINNEY, H.L. 2007 Experimental study of internal gravity waves generated by supercritical topography *Phys. Fluids* **19**, 096602.

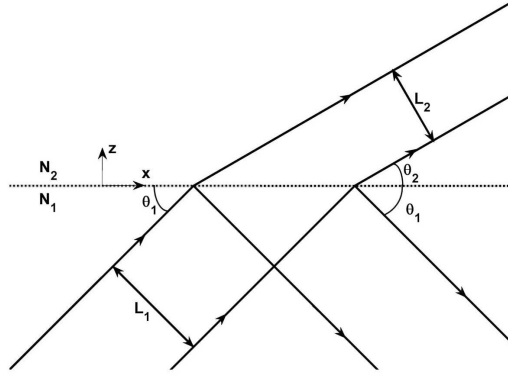


FIGURE 1. A sketch of the ray paths (solid black lines) for plane wave transmission from N_1 to N_2 across a sharp density-gradient interface (dotted black line). Refraction focuses energy flux from cross section L_1 to L_2 .

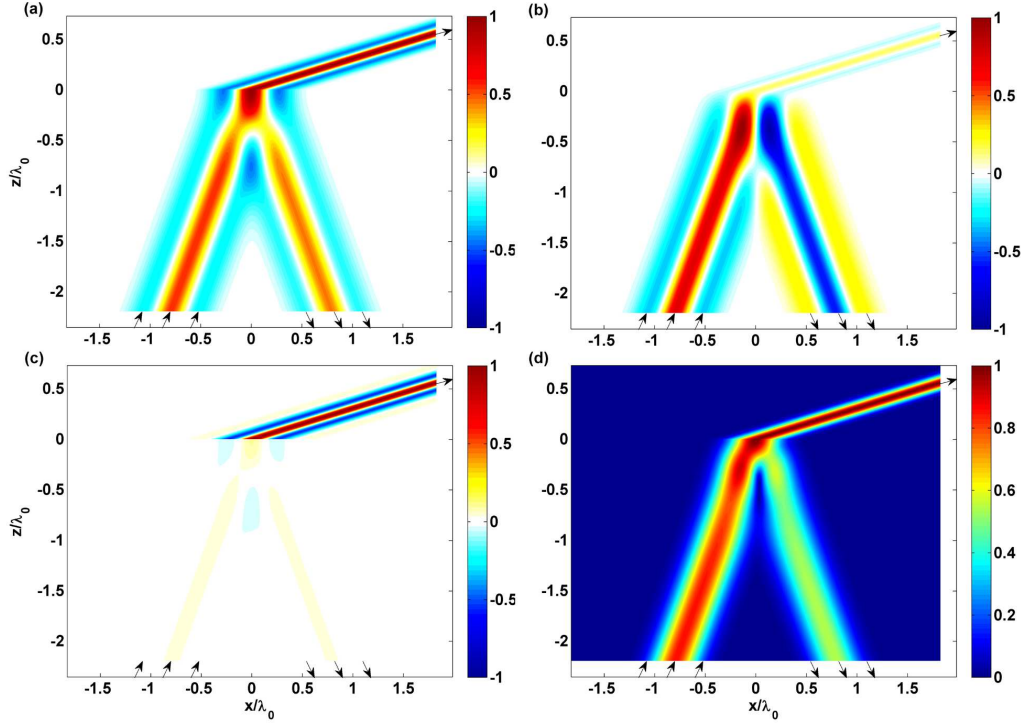


FIGURE 2. Wave beam transmission across a sharp density-gradient interface. (a) u . (b) w . (c) ΔN^2 . (d) \bar{e} . The frequency ratios are $\omega/N_1 = 0.94$ and $N_2/N_1 = 3.2$. Arrows specify the direction of energy propagation. The maximum value in each figure is scaled to unity, and the spatial scales have been nondimensionalized by the dominant wavelength, λ_0 , in $\psi_I(k)$. The dominant wavelength is defined as $\lambda_0 = 2\pi/k_0$, where $\psi_I(k)$ is maximum at $k = k_0$.

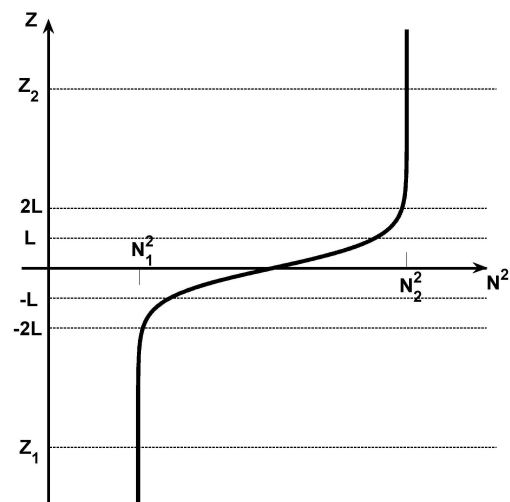


FIGURE 3. The N^2 -profile (3.1) considered for studying plane wave propagation across a finite-width transition region.

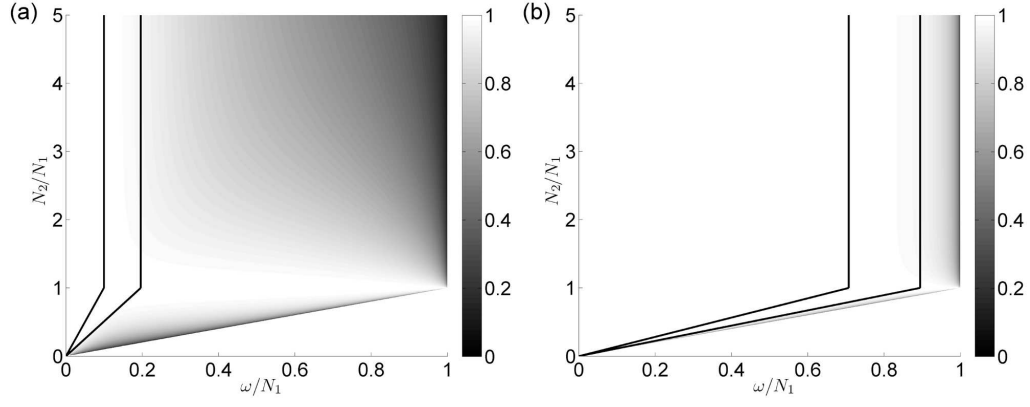


FIGURE 4. The transmission coefficient T_e for plane waves passing from N_1 to N_2 across a finite-width transition region. (a) $Lk = 0.1$. (b) $Lk = 1$. From right to left, the black line contours correspond to $Lk \min(\cot \theta_1, \cot \theta_2) = 0.5$ and 1, respectively.

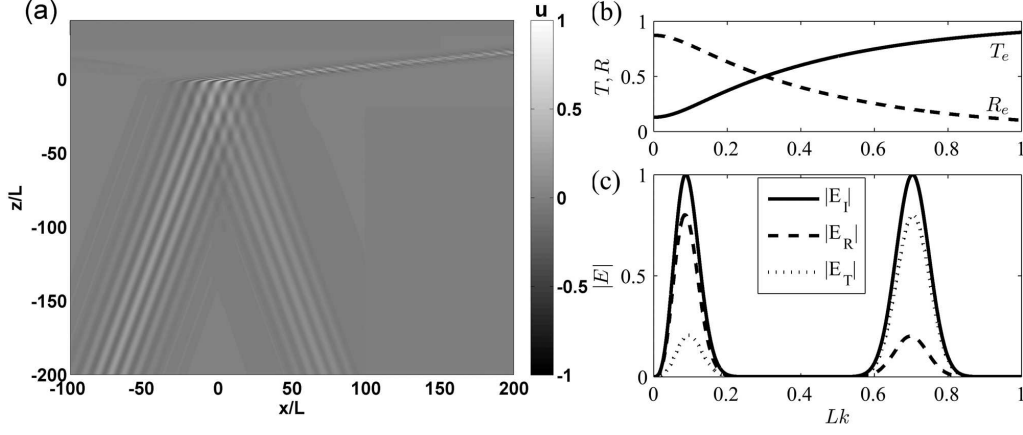


FIGURE 5. Filtering of an internal wave beam by a finite-width transition region. (a) The horizontal velocity field u at an arbitrarily chosen phase. The maximum value is scaled to unity, and the spatial dimensions are scaled by the interface length-scale L . (b) The plane wave reflection and transmission coefficients as a function of Lk . (c) The energy spectrum $|E(k)| = k|\Psi|^2 \cot \theta$ for the incident (I), transmitted (T) and reflected (R) wave beams. The values of ω/N_1 and N_2/N_1 are 0.94 and 10 respectively.

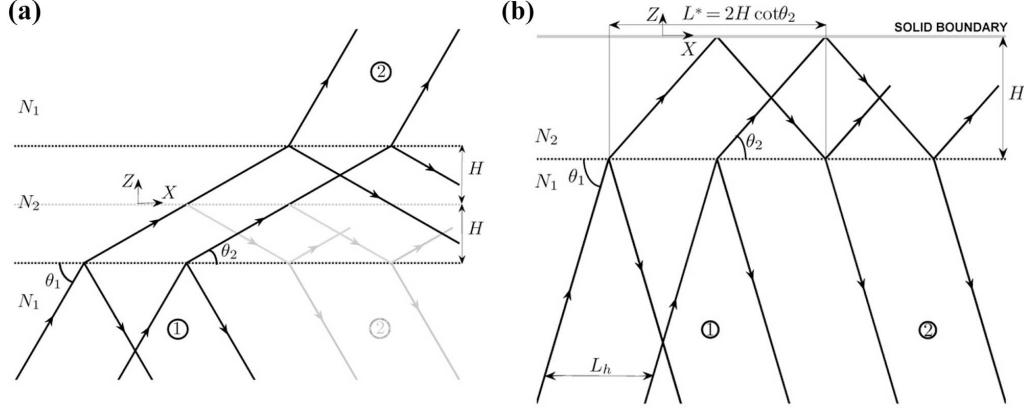


FIGURE 6. (a) Wave beam transmission across an N_2 -layer, which can be related to the finite-depth scenario in figure (b), as indicated by the light grey lines. (b) Wave beam transmission across a sharp density-gradient interface between an N_1 -medium and a finite-depth N_2 -layer. Solid black lines are ray paths that bound the wave beam and the dotted black lines are the interfaces. The first two emerging wave beams are numbered 1 and 2, respectively. The horizontal distance a ray travels between encounters with an interface is $L^* = 2H \cot \theta_2$.

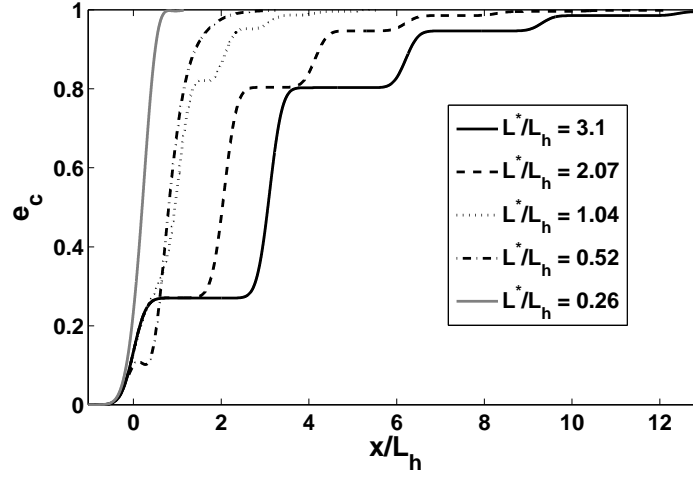


FIGURE 7. Cumulative energy e_c in reflected wave field (normalized by the energy flux in the incident wave beam) as a function of x/L_h for varying L^*/L_h . The parameter values are $\omega/N_1 = 0.5$, $N_2/N_1 = 2.8$.

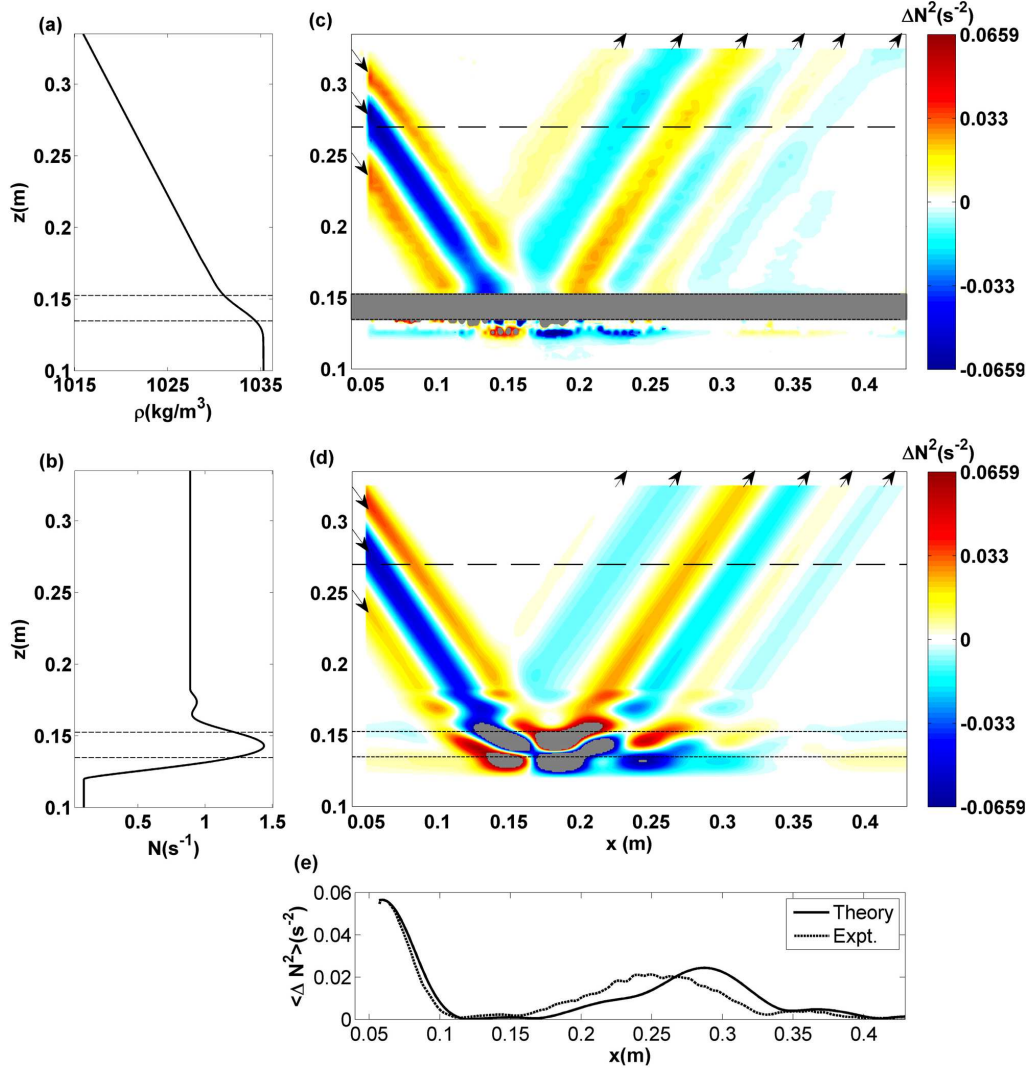


FIGURE 8. (a) Measured density profile. (b) Corresponding N profile. (c) Experimental ΔN^2 field obtained using Synthetic Schlieren for $\omega/N_1 = 0.82$. (d) Theoretical ΔN^2 field obtained by numerically solving equation (3.3). Regions with values outside the limits of the colorbar or where experimental data was not reliable due to strong stratification are grey. The arrows indicate the direction of local energy propagation, and the dashed lines indicate the horizontal section where the experimental and theoretical solutions are compared in (e). (e) Theoretical (solid) and experimental (dotted) amplitude envelope of ΔN^2 for the horizontal sections marked in (c) & (d).

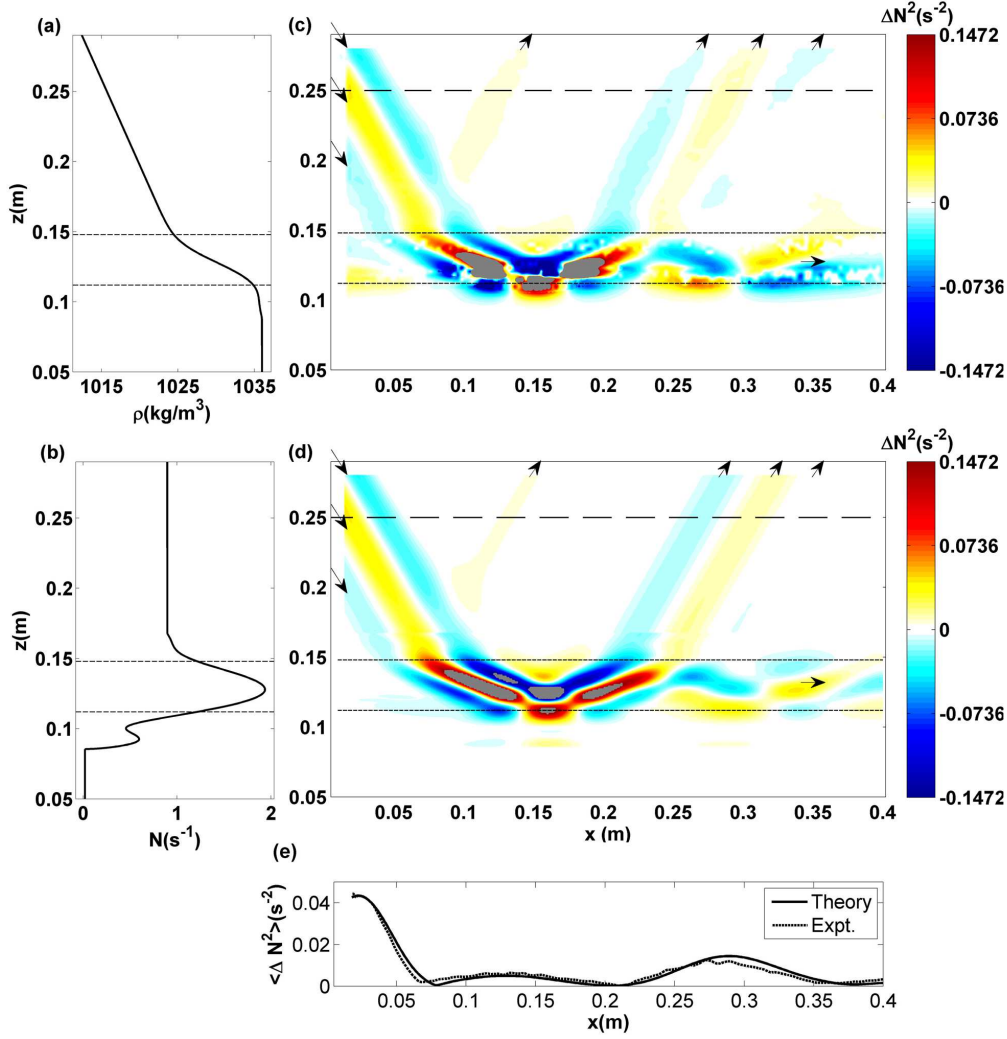


FIGURE 9. (a) Measured density profile. (b) Corresponding N profile. (c) Experimental ΔN^2 field obtained using Synthetic Schlieren for $\omega/N_1 = 0.87$. (d) Theoretical ΔN^2 field obtained by numerically solving equation (3.3). Regions with values outside the limits of the colorbar are grey. The arrows indicate the direction of local energy propagation, and the dashed lines in (c) & (d) indicate the horizontal section where the experimental and theoretical solutions are compared in (e). (e) Theoretical (solid) and experimental (dotted) amplitude envelope of ΔN^2 for the horizontal sections marked in (c) & (d).

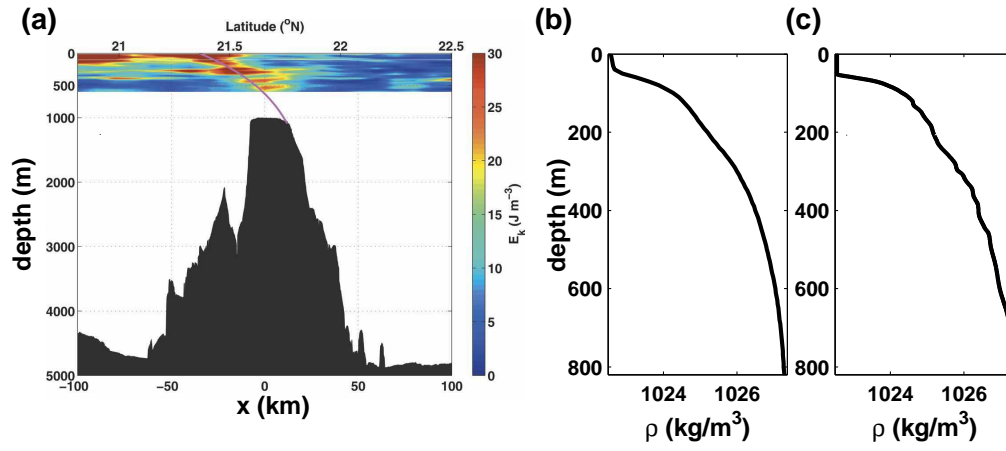


FIGURE 10. (a) The quantity E_k reveals the existence of an internal wave beam generated at the Keana Ridge (image reproduced from Martin *et. al.* 2006). (b) A time-averaged average density profile from the Keana ridge at the time of the data in (a). (c) An individual density profile from the Keana ridge during the time of the data in (a).

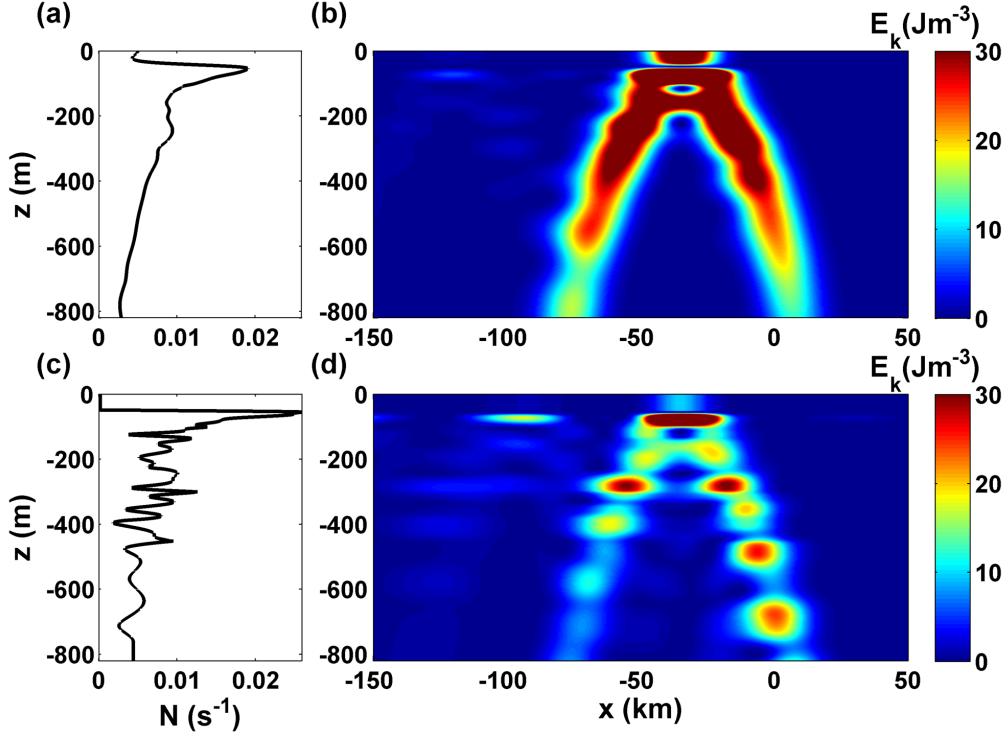


FIGURE 11. (a) The stratification for the time-averaged density profile in figure 10(b). (b) The quantity E_k for a simulated wave beam dominated by a 15km horizontal wavelength propagating through the stratification shown in (a). (c) The stratification for the individual density profile in figure 10(c). (d) The quantity E_k for a simulated wave beam dominated by a 15km horizontal wavelength propagating through the stratification shown in (c).

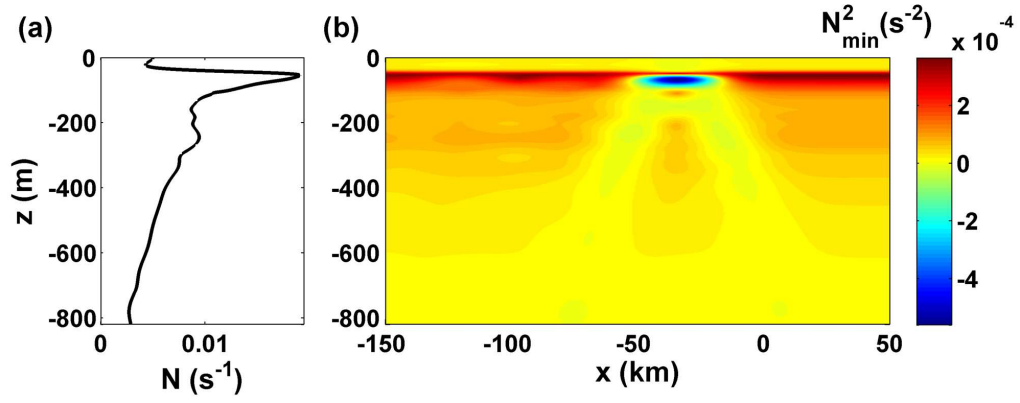


FIGURE 12. (a) The stratification for the time-averaged density profile in figure 10(b). (b)

N_{\min}^2 for the wave beam in figure 11(b). $N_{\min}^2 < 0$ indicates gravitational instability.